Physics of Fluids

Surface anchoring mediates bifurcation in nematic microflows within cylindrical capillaries

Cite as: Phys. Fluids **33**, 072005 (2021); https://doi.org/10.1063/5.0050379
Submitted: 15 March 2021 • Accepted: 03 June 2021 • Published Online: 12 July 2021

Paul Steffen, Eric Stellamanns and Anupam Sengupta

Physics of Fluids ARTICLE scitation.org/journal/phf

Surface anchoring mediates bifurcation in nematic microflows within cylindrical capillaries

Cite as: Phys. Fluids **33**, 072005 (2021); doi: 10.1063/5.0050379
Submitted: 15 March 2021 · Accepted: 3 June 2021 ·
Published Online: 12 July 2021

Paul Steffen,[1,a)] Eric Stellamanns,[2,a)] and Anupam Sengupta[1,b)]

AFFILIATIONS

[1]Physics of Living Matter, Department of Physics and Materials Science, University of Luxembourg, L-1511 Luxembourg City, Grand Duchy of Luxembourg
[2]Deutsches Elektronen-Synchrotron DESY, Notkestraße 85, 22607 Hamburg, Germany

[a)]Electronic addresses: steffen.science@gmail.com and e.stellamanns@gmail.com
[b)]Author to whom correspondence should be addressed: anupam.sengupta@uni.lu

ABSTRACT

Capillary microflows of liquid crystal phases are central to material, biological and bio-inspired systems. Despite their fundamental and applied significance, a detailed understanding of the stationary behavior of nematic liquid crystals (NLC-s) in cylindrical capillaries is still lacking. Here, using numerical simulations based on the continuum theory of Leslie, Ericksen, and Parodi, we investigate stationary NLC flows within cylindrical capillaries possessing homeotropic (normal) and uniform planar anchoring conditions. By considering the material parameters of the flow-aligning NLC, 5CB, we report that instead of the expected, unique director field monotonically approaching the alignment angle over corresponding Ericksen numbers (dimensionless number capturing viscous vs elastic effects), a second solution emerges at a threshold flow rate (or applied pressure gradient). We demonstrate that the onset of the second solution, a nematodynamic bifurcation yielding distinct director configurations at the threshold pressure gradient, can be controlled by the surface anchoring and the flow driving mechanism (pressure-driven or volume-driven). For homeotropic surface anchoring, this alternate director field orients against the alignment angle in the vicinity of the capillary center; while in the uniform planar case, the alternate director field extends throughout the capillary volume, leading to reduction of the flow speed with increasing pressure gradients. While the practical realization and utilization of such nematodynamic bifurcations still await systematic exploration, signatures of the emergent rheology have been reported by the authors previously within microfluidic environments, under both homeotropic and planar anchoring conditions.

I. INTRODUCTION

As we continue pushing the boundaries of miniaturizing functional materials for both synthetic and biological applications, there is a growing need to better understand the dynamics and response of such materials at small scales (typically, micrometer and sub-micro scales). Liquid crystals (LCs), since their discovery in the late nineteenth century, have been at the forefront of scientific and technological breakthroughs over the last century, revolutionizing the way we see, sense, feel, touch and think.[1–4] From novel metamaterials and optofluidic based applications,[5–8] to biological sensing and drug development,[9–11] LCs are now an integral part of our daily lives, in more ways than we can perceive. A vast majority of these life-changing applications rely on the dynamic interaction of LCs—from molecular to microscopic scales—with their environments, mediated by the local pressure, boundary and confinement conditions.[12–14] In addition to the confinement and surface anchoring, external fields play a key role in tuning the dynamic functionalities of LC materials. Hydrodynamic, electric and magnetic—the commonly studied external fields—have been central to the development of LC physics and applications, eliciting plethora of exotic dynamic attributes otherwise not observed in isotropic systems.[16–23]

Our ability to potentially harness these dynamical attributes relies on an unambiguous characterization of the microscale rheological properties of LC-s.[13,14] However, as demonstrated over the course of development of the field, such applied interest could often lead to fundamental insights, offering a rich landscape of unexpected dynamic manifestations, including generation[16] and sustenance[22,24] of transverse pressure gradients, anomalous viscoelasticity[25,26] and emergent biaxiality[27] and tunable flow shaping.[28] A key determinant of the effective rheological properties is the LC backflow mechanism, which has

only recently been characterized in microfluidic setups,[28,29] with potentially far-reaching ramifications in active and biological systems.[30–32] LC-s present distinct material advantages, thanks to the backflow-mediated coupling, over the isotropic counterparts. A coherent theory, with major contributions from Leslie, Ericksen, and Parodi (LEP) were achieved in the 1960s. Despite almost immediate confirmation of the theory, the lack of computing power and experimental control had long hindered a more detailed understanding of even simplified stationary flow configurations. In the last two decades, these barriers have eased which enabled growing progress. LC microfluidics, in tandem with advanced computing tools, has allowed unprecedented insights through controlled flow experiments within channels spanning different surface, confinement and hydrodynamic constraints.[13]

Though the advent of LC microfluidics has propelled our understanding of the microscale LC flow behavior, a bulk of the existing literature focuses on flows within channels with rectangular cross sections,[21,28] revealing topologically distinct director profiles separated by transition flow speeds. However, a closer look at the natural systems would reveal that ubiquity of the cylindrical geometry, across a wide spectrum of biological and technological settings. Yet, studies on the flow within circular cross sections (e.g., cylindrical capillaries) are relatively rare, thus necessitating the studies we have undertaken here. The significance of LC flows in cylindrical micro-capillaries, under natural and imposed constraints, have been demonstrated by the groups of Rey,[33–36] Sluckin,[37] and Yeomans,[38,39] with a growing relevance of these studies in a range of applied and fundamental settings, both in the context of passive and active material systems.[40–43] Rey and co-workers have studied capillary Poiseuille flows using the Leslie–Ericksen–Parodi (LEP) theory for discotic nematic liquid crystals (NLC-s).[35] Denniston *et al.*[38] and Batista *et al.*[40] performed Lattice–Boltzmann simulations allowing variations of the order parameter and obtained this transition as well, together with a shear thinning for the large flow velocity regime, while Ravnik and Yeomans[39] have used lattice Boltzmann simulations of Landau–de Gennes orientation tensor model to explore the behavior of active liquid crystals under Poiseuille flows. The LEP-based computations by Anderson *et al.*[41] confirmed experimental observations of different flow-induced director states,[28] and explained the underlying energetics of the transitions between the director configurations. Zhou and Forest have studied capillary Poiseuille flows using the Doi–Marrucci–Greco model employing a second-moment tensor description of the orientation distribution.[44]

A unified description of nematodynamics, bridging the existing gap between the classical LEP theory and the Doi theory, was first proposed by Tsuji and Rey.[33] By accounting for the relative contribution of the short- and long-range elasticities in shear flows, quantified as their ratio, R (reactive parameter), the authors presented a rheological phase diagram with four distinct regimes under fixed planar director boundary conditions, spanning Deborah (De) and Ericksen (Er) numbers. Of the four regimes, the elastic-driven steady state corresponds to the LEP solution for the non-aligning nematics, while the viscous-driven steady state corresponds to the flow aligning behavior at higher Er numbers. Since the two dimensionless numbers respectively capture the ratio of the viscous to short range elastic effect (De) and the ratio of the viscous effect to long-range elastic effect (Er), their mutual ratio results to the Reactive parameter, $R = Er/De$. The asymptotic limits of the in-plane shear flows yield the LEP theory (for $R \to \infty$) and the Doi theory (for $Er \to \infty$). Employing a Landau–de Gennes model, Alonso *et al.* studied Couette flow of NLC-s using asymptotic methods and numerical bifurcation theory.[37] In addition to confirming the four regimes, their results highlighted the existence of a Takens–Bogdanov point, a high-order singularity at the coincidence of a Hopf bifurcation and a limit point. It may be worthwhile to note that the applied technological interest (in particular, the processing of high performance fibers and films) which has guided investigations on the dynamical rheology of LC-s, has mostly focused on LC polymer materials under Poiseuille flows. However, complementary investigations on the flow of non-polymeric LC materials within cylindrical capillaries are still underexplored. The lack of systematic micro-scale studies of LC flows within cylindrical capillaries, or of the associated role of surface anchoring conditions (how LC molecules orient on the confining boundaries), offer opportunities to gain fundamental insights on dynamical states and nematodynamic bifurcations, with potential ramifications on the flow-structure coupling in a range of soft, active and biological systems.

In this paper we investigate stationary flows of NLC-s within cylindrical capillaries possessing strong homeotropic (normal) and uniform planar anchoring conditions using numerical simulations based on the continuum theory of Leslie, Ericksen, and Parodi (LEP theory). By spanning flow speeds over two orders of magnitude, we identify that at a threshold flow rate, a second flow-director solution emerges, in addition to the expected director field orientation. By systematically varying the Ericksen number [Eq. (1)] of our capillary flows *in silico*, we report experimentally tractable nematodynamic bifurcation points for nematic 5CB, as alternate solutions in the apparent viscosity emerge at the threshold pressure gradient. Although our simulations are carried out for a single capillary diameter ($2r = 831\ \mu$m) to reflect the dimensions in our ongoing experiments, the results presented here hold good for micrometer-scale cylindrical capillaries, with appropriate scaling of the relevant dimensionless numbers. We found that the bifurcation coordinates on a pressure–viscosity parameter space depend on the nature of surface anchoring on the walls of the cylindrical capillary, and on the driving mechanism of the flow. For strong homeotropic anchoring conditions, the flow bifurcation occurs at a pressure gradient of 14.7 Pa/m (flow rate 3.5 nl/s) and apparent viscosity 50 mPa s. In contrast, for the capillaries with planar boundary conditions, the bifurcation point is determined, in addition, by the driving mechanism of the flow, i.e., pressure-driven flows (constant pressure) vs volume-driven flows (constant volume rate). For the pressure-driven flows, the bifurcation occurs at 5.9 Pa/m (corresponding flow rate is 2.2 nl/s) and apparent viscosity 31 mPa s; whereas for volume-driven flows, the bifurcation takes place at a flow rate of 1.8 nl/s (corresponding pressure gradient is 8 Pa/m) and an apparent viscosity of 51 mPa s. Overall, the anchoring-dependent onset of multiple solutions with differing apparent viscosities at a given pressure gradient (or flow rate) can be coupled to the alternate local director orientations with similar energy costs.[24] For homeotropic surface anchoring, the second director field orients against the alignment angle close to the capillary center; while in the uniform planar case, the alternate director field extends throughout the capillary volume. Although experiments to systematically capture the simulated bifurcations are under way, signatures of the same could be found in author's previous works.[28,45]

II. THEORETICAL BACKGROUND

Based on the Frank theory of LC-s,[46] Ericksen, Leslie and Parody proposed a continuum theory for nematic flows, taking viscosity as

well as the interaction between flow and director field into account. In the following, we will refer to it as the LEP.[47–49] Its dominant parameter is the Ericksen number, *Er*:

$$Er = \frac{\eta \cdot v \cdot L}{k}, \tag{1}$$

where η, v, L, and k are the characteristic dynamic viscosity, flow speed, length scale, and elasticity. For small *Er* numbers, the elastic interactions dominate, for large numbers the viscous ones. A predicted shear alignment angle of the director field in the limit of high *Er* numbers—the Leslie angle—was confirmed through experiments in Couette flow using polarization optics by Gähwiller.[50] The Leslie angle depends on the material parameters as described in Sec. III. For stationary flows in cylindrical geometry, Atkin provided the ordinary differential equations which were used by Tseng *et al.* to calculate numerical solutions for the p-azoxyanisole and experimentally tested by Fishers and Fredrickson.[12,51,52] For homeotropic anchoring, the experimentally measured viscosity decreased monotonically with increasing Ericksen numbers. It scaled perfectly with *Er* for diameters between 78 and 516 μm and $20 < Er < 100\,000$. Using stationary Couette and channel flows, Pieranski and Guyon had demonstrated existence of multiple director configurations due to bifurcation under uniform planar anchoring with surface orientation perpendicular to the flow direction.[53–55] While Couette flows gave a quantitative agreement between the LEP and the experiments, for channel flows qualitative agreement with the LEP was concluded.[56–58] By employing non aligning nematics, oscillating flow and electric fields or magnetic fields, several further instabilities and bifurcations were obtained. The work by Lima and Rey[35] is worth mentioning as it numerically captures the stationary states of flowing discotic nematics within a cylindrical geometry, uncovering a plethora of nonlinear phenomena *in silico*, including shear thinning and thickening, distinct viscosity maxima and minima, as well as multiple stable solutions with mutually different slope signs.

The present investigation follows up on the work of Lima and Rey,[35] to specifically capture the flow behavior of rod-shaped NLC-s flowing within a cylindrical capillary, the role of surface anchoring on such microscale flows, and the possible dependence of the flow states on the driving mechanisms of the flow (pressure- vs volume-driven). Based on our understanding of the existing gaps, we have chosen study rod-shaped NLC-s, which possess fewer degrees of freedom than what has been reported for the discotic nematics. Through an in-depth numerical treatment of this basic system, the results of this work will provide a concrete perspective on designing and optimizing more complex cases and potential applications. With this in mind, we tackle the NLC flow problem along the lines of the work by Lima and Rey, however for rod shaped NLC-s (instead of discotic ones) flowing under different anchoring conditions.

III. METHODS AND MATERIALS

The flow geometry in our work is sketched in Fig. 1. We capture the flow dynamics by solving two ordinary differential equations obtained directly from the LEP by Atkin[51] under the assumptions described in Sec. III A. The capillary diameter, flow rates and the material properties of our system are chosen to reflect those in our experiments, which will be reported in a forthcoming paper. The paper is organized in the following manner: In Sec. III, we describe the

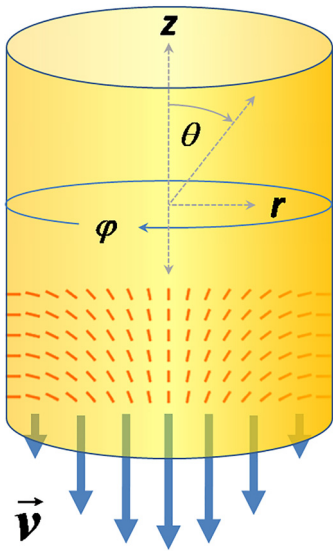

FIG. 1. Flow geometry and anchoring. The investigated geometry is a cylindrical micro-capillary, shown here with the employed spherical coordinate system. The symmetry axis of the capillary is denoted by *z*, the radial distance from this axis by *r*, the tilt angle relative to the symmetry axis by θ, and the azimuthal angle by φ. The red line-segments shown in the lower half of the capillary indicate the orientation of the rod shaped 5CB molecules, and the blue arrows at the bottom present the flow direction.

equations governing our numerical simulations (Sec. III A), the material parameters applied (Sec. III B), and finally our numerical treatment (Sec. III C). Section IV is divided into Sec. IV A for strong homeotropic anchoring and Sec. IV B for strong uniform planar anchoring oriented along the flow direction. For both anchoring types, we present the director fields, the shear rates and the apparent viscosities at Ericksen numbers spanning the elastic and the viscous regimes. In Sec. V A, we discuss the implications and plausibility of the solutions obtained, and Sec. V B gathers existing experimental evidence of our solutions. Finally, we conclude the paper in Sec. VI and provide a short perspective on potential applications of our findings.

A. Equations to solve

The geometry and the relevant coordinate system are described in Fig. 1. Following Atkin,[51] we apply the following conditions on the flow velocity $\vec{v}$ and the director field $\vec{n}$:

$$v_r = 0 \quad v_\varphi = 0 \quad v_z = v(r), \tag{2}$$

$$n_r = \sin(\theta(r)) \quad n_\varphi = 0 \quad n_z = \cos(\theta(r)), \tag{3}$$

where $\theta(r)$ is the director tilt with respect to the symmetry axis z of the capillary. This ansatz satisfies the continuity equation, i.e., it implies incompressible flow, and further imposes axial symmetry with vanishing φ-component for $\vec{n}$ and $\vec{v}$, leads to the two governing equations:[51,52]

$$g(\theta)v'(r) = -\frac{ar}{2}, \tag{4}$$

$$2f(\theta)\theta''(r)+f'(\theta)\left(\theta'(r)\right)^2+\frac{2}{r}f(\theta)\theta'(r)-\frac{k_{11}}{r^2}\sin(2\theta)+ar\lambda_2\frac{\cos(2\theta_0)-\cos(2\theta)}{2g(\theta)}=0, \tag{5}$$

with

- $2g(\theta)=2\mu_1\sin^2(\theta)\cos^2(\theta)+(\mu_5-\mu_2)\sin^2(\theta)+(\mu_6+\mu_3)\cos^2(\theta)+\mu_4,$ (6)
- $\mu_i=$ Leslie coefficients for the viscosity ($i=1$–6),
- $v'(r)=\frac{\partial}{\partial r}[v(r)]$ is the shear rate, and $v(r)$ the flow velocity, (7)
- a is a constant; due to Atkin[51] it denotes the axial pressure gradient dp/dz, where p denotes the pressure applied across the capillary;
- $f(\theta)=k_{11}\cos^2(\theta)+k_{33}\sin^2(\theta),$ (8)
- $k_{11}=$ splay elastic coefficient; $k_{33}=$ bend elastic coefficient,
- $\theta'(r)=\frac{\partial}{\partial r}[\theta(r)];\ \theta''(r)=\frac{\partial^2}{\partial r^2}[\theta(r)],$ (9)
- $f'(r)=\frac{\partial}{\partial r}[f(r)],$ (10)
- $\cos(2\cdot\theta_0)=-\frac{\lambda_1}{\lambda_2},$ (11)

  the aligning angle or Leslie angle, i.e., the limiting angle at large shear rates where elastic terms are negligible, and are dominated by the viscous terms;
- $\lambda_1=\mu_2-\mu_3=$ rotational viscosity, (12)
- $\lambda_2=\mu_5-\mu_6=$ torsional coefficient. (13)

Lima and Rey[35] gave an equivalent, regrouped and dimensionless version of Eqs. (4) and (5). In the static case, $a=v'(r)=0$ holds, for which an analytical solution could be obtained for Eq. (5).[60,61] The numerical evaluation of Eqs. (4) and (5) is described in Sec. III C. There we describe the applied boundary conditions and justify them, together with the restrictions imposed by the Eqs. (2) and (3).

B. Material parameters

The material parameters used here were obtained from Sengupta and Dhar *et al.*[24,61] The elasticities of the director field $\vec{n}$ for splay k_{11} and bend k_{33} are taken as 6.4 and 9 pN, respectively. The coefficients for twist and for saddle splay k_{22}, k_{24} do not show up in the final equations. For the Leslie coefficients μ_i we assumed in units of mPa s: $\mu_1=-6$; $\mu_2=-81.2$; $\mu_3=-3.6$; $\mu_4=65.2$; $\mu_5=64$; $\mu_6=-20.8$. If the resulting $\lambda_{1,2}$ satisfies the condition:

$$1<\left|\frac{\lambda_1}{\lambda_2}\right|, \tag{14}$$

the alignment angle described above cannot be real and the stationary solution ansatz followed here works only for small Ericksen numbers (with no stationary solution at high *Er*), signifying the tumbling NLCs. The material parameters introduced above lead to an aligning behavior with a Leslie angle of 11.89°.[24]

The term $g(\theta)$ in Eq. (4) is analogous to the viscosity in the corresponding equation in the Hagen–Poiseuille flow, except that it is dependent on the angle $\theta(r)$ and therefore on r as well, it is called anisotropic viscosity. Its dependence on θ, i.e., the tilt angle of the director, is plotted in Fig. 2. The value for $\theta=0°$ (director in the shear plane and perpendicular to the velocity gradient) is known as the Miesowicz viscosity, $\eta_1=\frac{1}{2}(\mu_3+\mu_4+\mu_6)=20.4$ mPas for our chosen material. The value for $\theta=90°$ (director in the shear plane and parallel to the velocity gradient), corresponds to the Miesowicz viscosity, $\eta_2=\frac{1}{2}(\mu_4+\mu_5-\mu_2)$, with a value of 105.2 mPa s for our material.[24] The remaining Miesowicz viscosity (director perpendicular to the shear plane) can be computed as $\eta_3=\frac{1}{2}\mu_4$, with a value of 32.6 mPa s for our chosen material. The corresponding shear is however prohibited by the symmetry assumptions Eqs. (2) and (3).

The coefficients k_{ii} and η_i represent the anisotropy of the NLC, and thus should be appropriately accounted for computing the Ericksen number in Eq. (1). Because the elastic coefficients k_{11}, k_{33} are both always present in our configuration and μ_4 represents the isotropic Leslie coefficent, with the corresponding viscosity comparably less dependent on the temperature, we choose $k=k_{11}+k_{33}$ as the characteristic elasticity and $\eta_3=\frac{\mu_4}{2}$ as the characteristic viscosity in Eq. (1). Finally, we choose our main capillary diameter (831 μm) as the characteristic length scale and the average velocity as the characteristic one, which cause the Ericksen numbers of the simulations to be 3.2 fold higher than the simulated flow rates in units of nl/s.

C. Numerical approach and validation

We considered two anchoring cases: in Sec. IV A, we investigate $\theta(r=R)=90°$, i.e., the homeotropic anchoring condition, and in Sec. IV B $\theta(r=R)=0°$, the uniform planar alignment with the surface anchoring parallel to the flow direction. Since $\theta(r=R)$ is not influenced by the slope of $\theta(r)$ in the neighborhood, strong anchoring holds in both cases. Additionally, we impose $\theta(r=0)=0°$ for both anchoring cases, i.e., the director field $\vec{n}$ is parallel to the capillary axis along the capillary center, as already imposed for $\vec{v}$ within the entire capillary due to Eq. (2). This approach follows Tseng *et al.*[52] and Lima and Rey,[35] alongside restrictions imposed by the Eqs. (2) and (3).

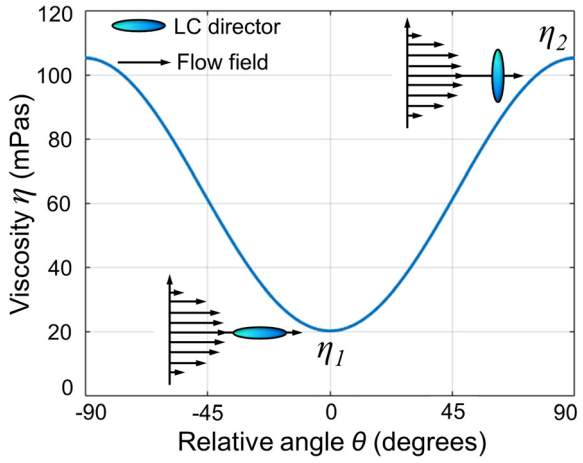

FIG. 2. Anisotropic viscosity. Due to the anisotropy of the viscosity coefficients, the apparent viscosity of the flowing NLC depends on the flow-induced director tilt angle. It is determined by the function $g(\theta)$ in Eq. (4). The Miesowicz viscosities η_1 and η_2 are described in the text and Refs. 15 and 24.

The calculations under the imposed restrictions have been previously validated and additionally, reproduced in experiments. The viscosities in cylindrical capillaries for homeotropic anchoring calculated by Lima *et al.*[35] were found to be in good agreement with the viscosimetric experiments by Fishers and Fredrickson.[12] The experiments varied the cylinder diameters between 78 and 516 μm, thus varying the Ericksen number as $20 < Er < 100\,000$. Additionally, small angle x-ray (SAXS) measurements on 5CB in cylindrical micro-capillaries, performed under homeotropic anchoring conditions by the authors,[62] have preliminarily revealed a close match between the average director field obtained from the scattering peaks and that from the computations. For very high Ericksen numbers, we expect the appearance of disclinations, and emergent fluctuations in the flow fields, as commonly observed in large *Er* channel flows.[63,64] For our investigations the Ericksen number is smaller than 500: this minimizes the possibility of disclination-mediated deviations from the imposed restrictions in our cylindrical capillaries.

We integrate Eq. (5) by using the conditions for θ at $r = 0$ and $r = R$ as boundary conditions. The resulting boundary value problem is converted into an initial value problem by using the shooting method,[65] through imposing θ and testing with θ' either at $r = 0$ or at $r = R$ until the desired adjacent angle is obtained. The first alternative was used to obtain solutions where the sign of θ changes within the integration range. Due to the properties of Eq. (5), we could not apply at $r = 0$, therefore we shifted the left boundary of the integration range from $r = 0$ to $r = \varepsilon$, with $0 < \varepsilon \ll R$. The corresponding flow rate $\dot{V}$ is then obtained from $\theta(r)$ by using Eq. (4) and applying the no slip condition $v(r = R) = 0$ at the surface of the capillary:

$$\dot{V} = 2\pi \int_0^R r \left\{ \int_R^0 \frac{ax}{2g(\theta(x))} dx \right\} dr. \tag{15}$$

The algorithm was programed using Matlab with the standard routine ode45 for the integration of Eq. (5). Checks with the software package Mathematica gave identical results. Lima and Rey[35] had undertaken a dimensionless equivalent of our equations Eqs. (4) and (5) using the finite element method, and computed them on material parameters corresponding to those of the discotic nematics.

We validated our method by plugging in the same parameters as Lima and Rey,[35] and reproduced their results for discotic nematics as visualized in Fig. 3. The top panels (a) and (b) correspond to the Figures 5(a) and 6(a), respectively, in Ref. 35, capturing the tilt angles (in radians) as a function of the radial position within the capillary under planar anchoring. The stark difference between the solutions shown in both the panels indicates existence of multiple solutions. Figures 3(c) and 3(d) present our solutions, exhibiting a close match; while the bottom panels (e) and (f) visualize corresponding director projections. Due to the material parameters chosen here for the discotic nematics, the Leslie angle is 1.157 rad, i.e., 66°, higher than for

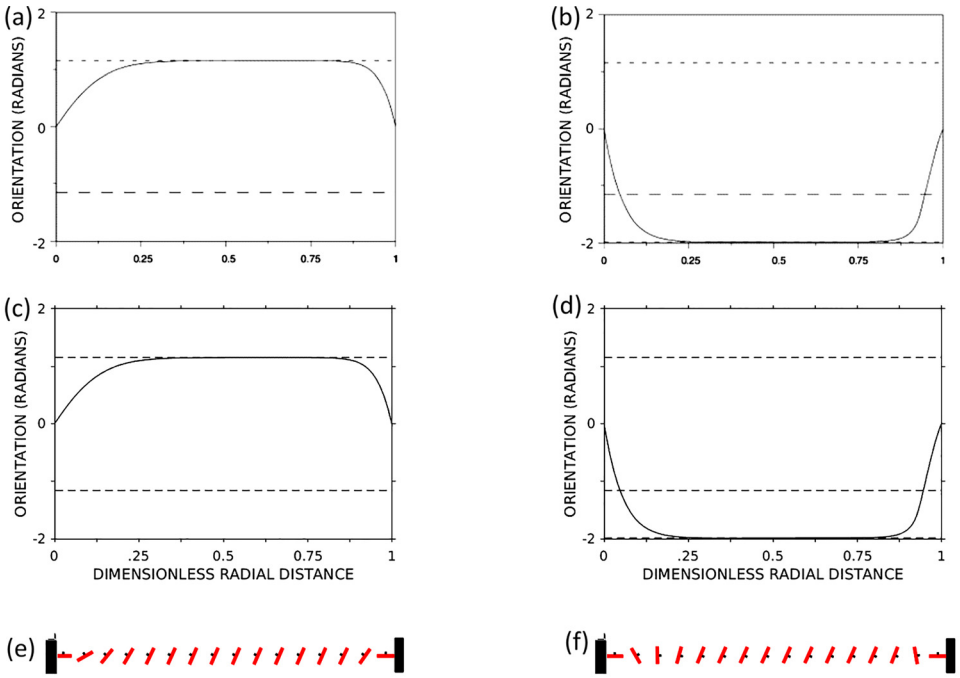

FIG. 3. Validation of our numerics. Multiple director tilt angles obtained for discotic nematics are shown in panels (a) and (b). Adapted with permission from Lima *et al.*, J. Non-Newtonian Fluid Mech. **110**, 103 (2003). Copyright 2003 Elsevier.[35] Corresponding results obtained using our algorithm, shown in panels (c) and (d), obtained by plugging in the same material parameters[35] into our computations. The reproduction shows a perfect matching with Ref. 35. On the left panels as well as on the right panels the anchoring is uniform planar, i.e., identical. Nevertheless, the tilt angles on the left panels are positive, while negative on the right ones, indicating the existence of multiple solutions. The bottom panels (e) and (f) visualize the director tilt angle plots above. For the disk like molecules visualized here, the tilt axis is parallel to the short axis, in contrast to the rod like molecules depicted in the other visualizations of this paper.

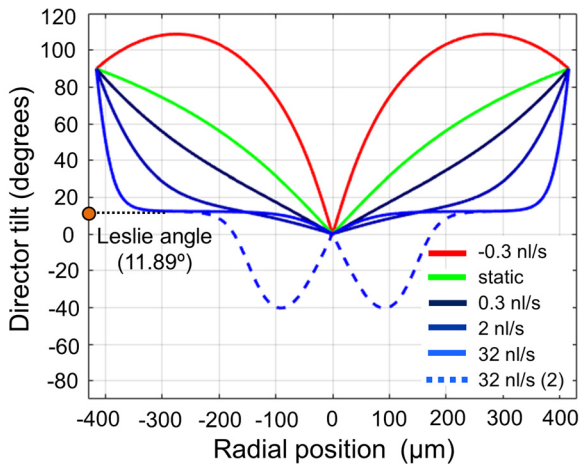

FIG. 4. Flow-induced director tilt under strong homeotropic anchoring. The spatial variation of the numerical director tilt angles $\theta(r)$, for strong homeotropic anchoring, are plotted for different flow rates shown with different hues (in units of nl/s, i.e., nanoliters/second). The corresponding Ericksen numbers *Er* are 3.2 times the flow rate in nl/s.

the nematic 5CB. The right-hand panels show the equilibrium tilt angle of -1.985 rad, i.e., $-114°$, which is equivalent to 66° due to the symmetry of the molecules. For the disk like molecules considered here, the tilt axis is parallel to the short axis of the molecules, in contrast to the rod like molecules depicted in the other visualizations of this paper, where the tilt axis is parallel to the long axis of the molecules.

IV. RESULTS

For an isotropic fluid one would expect a parabolic flow profile as for the classical Hagen–Poiseuille flows with the shear rate increasing strictly linear with the radial distance, r. A nematic phase pertubs this profile due to the uniaxial anisotropy. First, its effective viscosity at a given location depends on the angle θ between the director field and the flow direction. The anisotropic viscosity $\eta(\theta)$ given by the function $g(\theta)$ in Eq. (6) is plotted in Fig. 2, for the material parameters chosen here. Second, owing to the flow-director coupling, the flow field distorts the director field and at low Ericksen numbers, nematic backflow kicks in whereby the director field impacts the flow field. In Secs. IV A and IV B, we will describe the resulting director fields, shear rates and the emergent dynamic viscosity over different flow rates (Ericksen numbers) under strong homeotropic as well as strong uniform planar anchoring.

A. Homeotropic anchoring

Figure 4 presents the spatial variation of the flow-induced director field within the cylindrical capillary possessing strong homeotropic anchoring, i.e., the director at the surface is oriented strictly perpendicular to the surface. The resulting director tilt angles $\theta(r)$ are plotted for different flow rates (in units of nl/s, i.e., nanoliters per second), as indicated by the different legend hues. The corresponding director field for each case is presented by the panels in Fig. 5. The red line-segments in Fig. 5 indicate the variation of the director tilt angles, while the solid black line between the red line-segments quantify the local shear rates (the ticks and accompanying numbers indicate the shear rates in $1/s$). The two thick vertical black flanking either sides denote the capillary wall in each panel. As shown, the shear rate in the capillary center is always zero, which follows from Eq. (2) for a differentiable velocity profile. In the static case (flow speed of 0.0 nl/s), the shear rate is zero everywhere, as depicted in upper row of Fig. 5 (middle panel). Under homeotropic boundary conditions, two different nonsingular static director configurations can spontaneoulsy emerge within our capillaries (singular solutions are ruled out for capillary dimensions considered here): the "escape to the top" and the "escape to the bottom" configurations. The results presented in Figs. 4 and 5 focus exclusively on the bottom escape configuration. Positive (negative) flow rates denote the direction of the NLC microflow parallel (antiparallel) with respect to the escape direction.

The escape director field for the nematics at rest (green line in Fig. 4) is solely shaped from the competition of elastic forces, namely splay and bend, excluding twist due to the symmetry imposed by

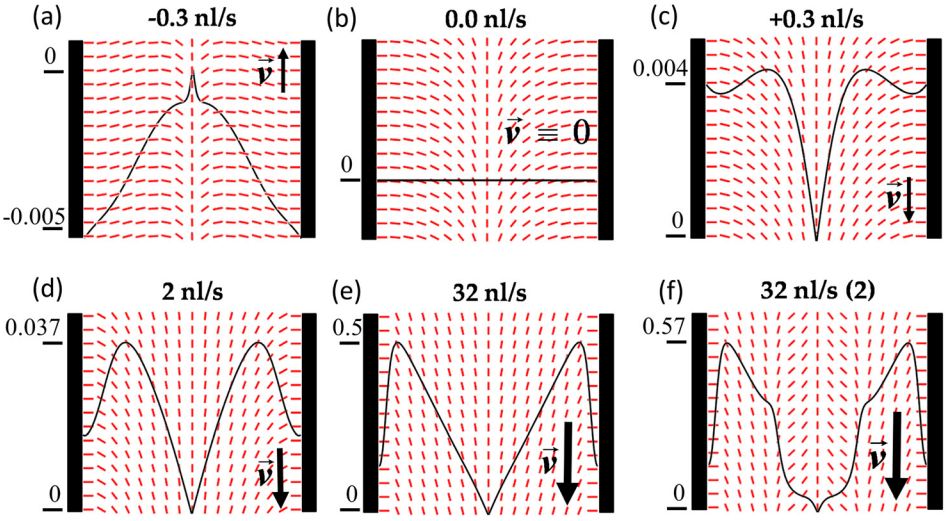

FIG. 5. Flow-induced director field and emergent shear rates (homeotropic anchoring). The red line-segments capture the flow-induced director tilt angle, corresponding to the conditions plotted at Fig. 4. The black line quantifies the emergent shear rates, which remains zero at the capillary center. The plots are normalized for having an equal maximum height, with the exception of the static case.

Eqs. (2) and (3). The shear involved in a moderate flow rate of ±0.3 nl/s already bends the director field, however the effect depends on the direction of the imposed flow relative to the escape direction. For positive flow rates, i.e., the flow is parallel to the direction of escape, the director configuration is pushed to lower angles (visualized in Fig. 5, upper row right panel), whereas for negative flow rates the director tilt reaches higher angles and a non monotonic dependence on r is captured (visualized in Fig. 5, upper row left panel). The negative flow rate induces a stronger director deformation than the positive one and is even able to orient the director field against the initial escape direction in the outer part of the capillary. The absolute value of the shear rate shows a strong slope in the immediate vicinity of the capillary center only, since $\theta(r)$ increases quickly and thereby, the anisotropic viscosity as well, with increasing r. At moderate positive flow rate (+0.3 nl/s), the director angle θ increases gradually which causes the flattening of the shear rate over larger distances from the capillary center. Near the surface, the gradient of the director tilt increases, as depicted in Fig. 4. This leads to local anisotropic viscosities which stabilize the maximum shear rate away from the capillary wall, between the centerline and the wall (Fig. 5, upper row right panel). The positive flow rates tilt angles $\theta(r)$ are further away from 90° which explains its lower viscosity compared to the negative flow rate shown in Fig. 10(a).

Upon increasing the flow rate to $\dot{V} = 2$ nl/s, the director tilts toward the flow direction, i.e., the tilt angles $\theta(r)$ decrease everywhere. This effect is stronger close to the confinement surfaces than at the center, where the shear rates are smaller and consequently, the shear-induced torques as well. In combination with the strong homeotropic anchoring condition, this results in stronger tilt angle gradients close to the surfaces, ultimately resulting in a sharper shear rate maximum, and relatively larger shear rate decay toward the surfaces (Fig. 5, lower row left panel). The apparent viscosity drops due to the smaller tilt angles as captured in Fig. 10(a), in agreement with the commonly observed shear thinning behavior.[45]

For $\dot{V} = 32$ nl/s, we found two different solutions. The first one, denoted by the solid line in Fig. 4 (light blue hue) shows a steady tilt angle of around $\theta_0 = 11.89°$, which does not vary further. θ_0 is called the Leslie angle, which can computed also from the Leslie coefficients α_i as described in Sec. III. For $\theta = \theta_0$, the viscous torque on the director approaches zero. The higher the Ericksen number, i.e., the shear rate, the closer the director orients to the Leslie angle (where the viscous torques become smaller and smaller) because then even this comparably weak viscous torque outbalances the elastic torque. Therefore, θ_0 is the limiting tilt angle at high Ericksen numbers, wherein the contribution of the elastic torque on the director configuration is negligible.[34,50] The second solution for $\dot{V} = 32$ nl/s, visualized by the blue dashed line, exhibits a non-monotonic dependence of the tilt angle on the local position within the capillary. The tilt angle dips to −40°, in agreement with previous reports.[52] The smallest flow rate which triggers the onset of this second solution is the point of nematodynamic bifurcation, which we found $\dot{V} = 3.5$ nl/s. The apparent viscosity corresponding to the two numerical solutions [shown in Fig. 10(a)], as well as the corresponding director fields, can be clearly distinguished at the bifurcation. At low flow rates, the two solutions do not meet there each other, in close agreement with the phenomenon reported by Lima and Rey for the stationary flow of discotic nematics within cylindrical capillaries.[35] For higher flow rates, the viscosities of the two solutions merge quickly together: at 5 nl/s, the two solutions can hardly be distinguished. We obtained the second solution up to our highest considered flow rates around $\dot{V} = 150$ nl/s. As visible in Figs. 4 and 5, the two director solutions (for 32 nl/s) are similar to each other in the outer parts of the capillary (large values of r), however vary considerably close to the capillary centerline. Consequently, the shear rates mirror the director fields, by showing strong differences at the capillary centerline.

B. Uniform planar anchoring

Figure 6 depicts our simulation results for the NLC flows within cylindrical capillaries possessing strong uniform planar anchoring, analogous to the results on the homeotropic case (presented in Fig. 4). The surface orientation of the nematic director is parallel to the flow direction. For this combination of geometry and anchoring condition, there is no spontaneous symmetry breaking at zero flow rates, thus we do not differentiate between positive or negative flow rates. The solutions presented in Fig. 6 are obtained under the condition:

$$\frac{\partial}{\partial r}(\theta(r)) \geq 0 \tag{16}$$

close to the capillary center. Spatially, the director tilt spans the surface-anchored orientation, 0°, to the equilibrium Leslie angle, ∼12°, thus covering a much smaller angular range relative to the homeotropic case. Overall, the spatial variation of the director tilt follows the same trend across the different flow rates, which are represented by differently hued plotted lines in Fig. 6. Complementing the spatial director tilt, Fig. 7 visualizes the corresponding shear rates for the static and dynamic cases (left and right panels respectively). At zero flow, the director field is completely uniform, and the shear rate- = 0. The higher the flow rates, the higher the tilt angles within the capillary, which gradually approach the Leslie angle as the flow rate is enhanced. At the highest flow rate shown here (128 nl/s), the director field is spatially aligned to the Leslie angle (red line in Fig. 6) almost

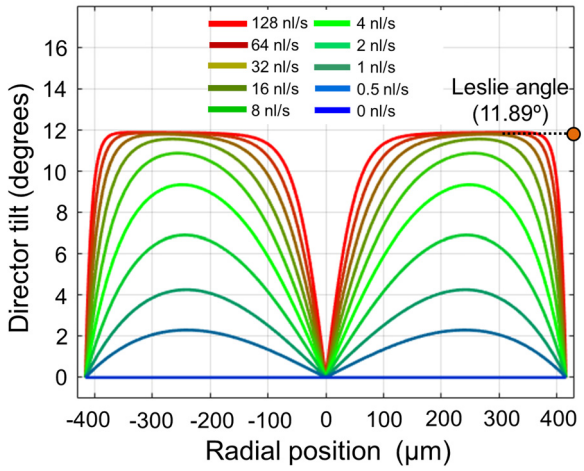

FIG. 6. Flow-induced director tilt under strong planar anchoring (positive tilt). Analogous to Fig. 4, the spatial variation of the director tilt is plotted over different flow rates. The maximum tilt angle in uniform planar anchoring is the Leslie angle, ∼12°, which is much smaller than the maximum flow-induced tilt angle under homeotropic anchoring conditions (110°, Fig. 4).

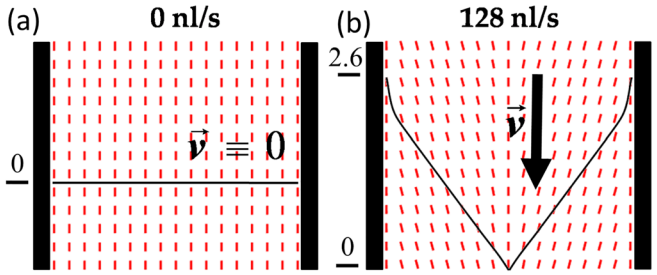

FIG. 7. Flow-induced director field and emergent shear rates (planar anchoring). For two of the flow rates in Fig. 6, static case (left panel) and 128 nl/s (right panel), the director tilt orientation is visualized by the red line-segments. The shear rates are denoted by the black lines overlaying the director tilt. The static case shows a completely homogenous director field, with zero shear rate. For the dynamic case (128 nl/s), the flow-induced change of the director tilt is rather small (from 0° to 12°), however a pronounced kink in the shear rate could be seen close to the wall due to the local backflow effect enhanced by the no-slip boundary conditions.

through the entire capillary, except at the neighborhood of $r = 0$ (along the centerline) and at $r = R$ (at the capillary wall) where the tilt angle is imposed to be zero (as discussed in Sec. III C). At the boundary and at the center, the angle drops with a certain slope down to zero, at the center with a smaller slope, due to the lower shear rates there. Similar director fields were reported for the Hagen–Poiseuille flow of discotic nematics under planar anchoring by Lima and Rey,[35] as depicted for a case in Fig. 3(a).

Owing to the pronounced role of backflow close to the capillary walls, this director configuration is reflected characteristically in the shear rate profile (Fig. 7, right panel). The simulated shear rate profile shows qualitative similarity with that of an isotropic fluid underdoing Hagen–Poiseuille flow, however two specific upward kinks appear here due to the flow-director coupling. The first kink is observed prominently close to the boundary (due to backflow), and a second minor upward kink is captured at the center due to the minute enhancement of local flow rate at the center (tilt ∼0°) relative to the vicinity where the tilt angle is ∼12°. The apparent viscosity and pressure gradients emerging within the planar flow configurations are plotted in green hue in Figs. 10(a) and 10(b) (denoted by the legend *planar anchoring, positive tilt angles*). Due to the increase in the tilt angles with increasing flow rates, the viscosity in this case shows a small positive slope. The slope is comparatively large at small flow rates and shrinks for larger flow rates, finally saturating to constant viscosity as the director tilt reaches the Leslie angle.

In Fig. 8, we present the computed director and emergent shear rate profiles for the complementary uniform planar case, as given by:

$$\frac{\partial}{\partial r}(\theta(r)) \leq 0 \tag{17}$$

around the capillary centerline. For the smallest flow rate (1.83 nl/s), we obtain a steep negative gradient of the tilt angle around the capillary centerline, accompanied by a more gradual negative tilt angle, with a minimum tilt at around −120° located at a distance of 200 μm from the center. Due to the anchoring condition, the tilt angle increases steeply after this minimum, ultimately reaching 0° at the centerline. The director configuration suggests strong elastic deformations, which couple with the flow field to lead to a complex shear rate

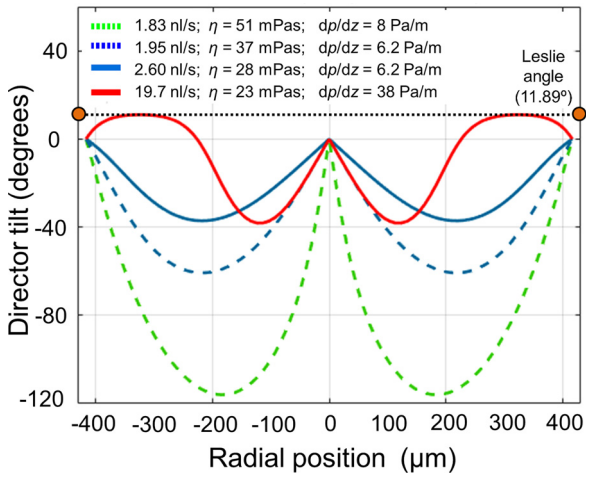

FIG. 8. Flow-induced director tilt under strong planar anchoring (negative tilt). Analogous to Fig. 6, the plot presents uniform planar anchoring with negative tilt angles in the vicinity of the capillary center. The maximum tilt angle here is the alignment angle, around 12° which is the same as in Fig. 6. The minimum tilt angle is strongly negative, ∼−120°, leading to a large angular span of the director tilt.

profile shown in Fig. 9 (upper left panel). Upon increasing the flow rate to 1.95 nl/s, we capture a similar trend, however with considerably weaker slopes (Figs 8 and 9, upper right panel). On average, the tilt angles for the larger flow rates deviate further from 90°, i.e., the anisotropic viscosities due to Fig. 2 are smaller for them. Thus, one expects a lower apparent viscosity for a flow rate of 1.95 nl/s (37 mPa s) than at 1.83 nl/s (51 mPa s), as demonstrated in Fig. 8 by the green dashed and blue dashed plots. Interestingly, when we look at the resulting

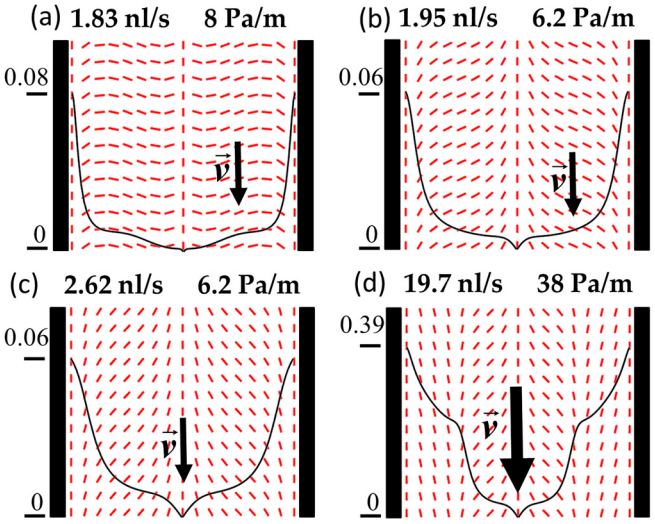

FIG. 9. Flow-induced director field and emergent shear rates (planar anchoring). Director field and emergent shear rates for negative the tilt angles in the vicinity of the capillary center. For each of the four plots in Fig. 8, the orientation of the director field is visualized by the orientation of red line-segments. The shear rates are denoted by the black lines overlaying the director field.

pressure gradient, we can conclude that the higher the flow rate, the lower is the pressure gradient (8 Pa/m for lower flow rate vs 6.2 Pa/m for the higher flow rate). Such stationary flow characteristics have, to the best of our knowledge, been reported for the first time here. A nematodynamic regime in which the pressure drops when the flow rate increases can reach stationary flow state only if the flow rate is externally imposed. If external pressure is imposed (pressure-driven flows), the system turns unstable, as presented in the apparent viscosity vs pressure gradient plot in Fig. 10(b) (red hue, planar anchoring with negative tilt angle). The onset of this solution type is above zero, at ∼1.8 nl/s [Fig. 10(a)], resulting in a bifurcation for the uniform planar anchoring case with its branches having different viscosities, i.e., the two branches do not meet each other. The unstable part, where the pressure gradient drops with increasing flow rates, is shown with dotted lines. For higher flow rate, the viscosity drops further, with its slope decreasing continuously until it meets the saturated viscosity which essentially corresponds to the expected first solution shown in Fig. 6.

Figure 10 illustrates how the nature of the bifurcation, i.e., the director topology—manifested as the apparent viscosity and emergent pressure gradients—changes as function of the flow rate and direction (for the homeotropic case), and captures the dynamical solutions as a function of the input control parameter, the flow rate. The existence of nematodynamic bifurcation signifies a dynamical transition from one to two solutions. As presented in Fig. 10(b), the pressure gradient is plotted as the input, the output parameter being the flow rate. Here one observes a clear transition from one to three solutions. As shown in Figs. 8 and 9, at 2.6 nl/s the pressure is equal to the pressure at the previous flow rate of 1.95 nl/s, plotted using a solid line to indicate that this flow is stable. The pressure gradient increases with increasing flow rates, while the viscosity keeps dropping further. The absolute values of the director tilt angle are smaller than those at smaller flow rates, which is expected due to the decreased apparent viscosity. The largest flow rate depicted in Fig. 8 (19.7 nl/s) interrupts the hitherto increase in the tilt angle slope at the capillary centerline for increasing flow rates. Instead, the negative slope recovers again, reaching values comparable to those for the flow rate of 1.95 nl/s. Spatially, the tilt angle reaches its minimum close to the centerline, at $r \approx 150\ \mu$m, thereafter increasing sharply to cross the zero tilt angle at $r \approx 226\ \mu$m away from the center. Finally, the director tilt reaches its maximum of ∼12°—the Leslie angle—until it drops back to 0° at the capillary boundary. As shown in Fig. 10(a), the apparent viscosity drops further, ultimately matching with the apparent viscosity corresponding to the positive tilt angle solution at the same flow rate.

The shear rates shown in Fig. 9 can be interpreted as those presented for the Figs. 5 and 7. At regions with zero tilt angles (imposed at the capillary center and at the boundary), one expects the slope of the shear rates to be higher relative to the slopes within rest of the capillary. This is clearly captured in Fig. 9, in contrast to Fig. 5 (lower panels) where the homeotropic anchoring partially causes negative slopes of shear rate near the capillary boundary. At the capillary center, the slope is clearly high for the latter three flow rates. The quicker the tilt angles increase, the tighter is the central region with stronger slopes, owing to the increased anisotropic viscosity due to higher tilt angles. Figure 10(a), furthermore, indicates that the apparent viscosities for the two distinct anchoring states—homeotropic and uniform planar—converge at higher flow rates, in agreement with previous experiments.[45] Second, for the homeotropic case, one needs to distinguish between the escape configurations of the director field observed. The spontaneous symmetry breaking in the flow-director coupling elicits distinct apparent viscosities corresponding to the positive flow rates (escape direction parallel to flow direction) and the negative flow rates (escape direction antiparallel to flow direction), even for the same *Er* number. At small negative flow rates the viscosity initially goes up with the magnitude of the flow rates, before it starts to decrease. Under uniform planar anchoring, no such flow-director asymmetry exists: consequently, the apparent viscosity remains similar regardless whether the flow started along or opposite to the capillary axis (*z*-axis).

V. DISCUSSION

A. Plausibility of the negative tilt angle solutions

For flow-aligning NLC-s like 5CB, the viscous torque tends to align the director field toward the Leslie angle in the viscous dominated regime, i.e., at high *Er*.[47–49] However, deviations from the Leslie

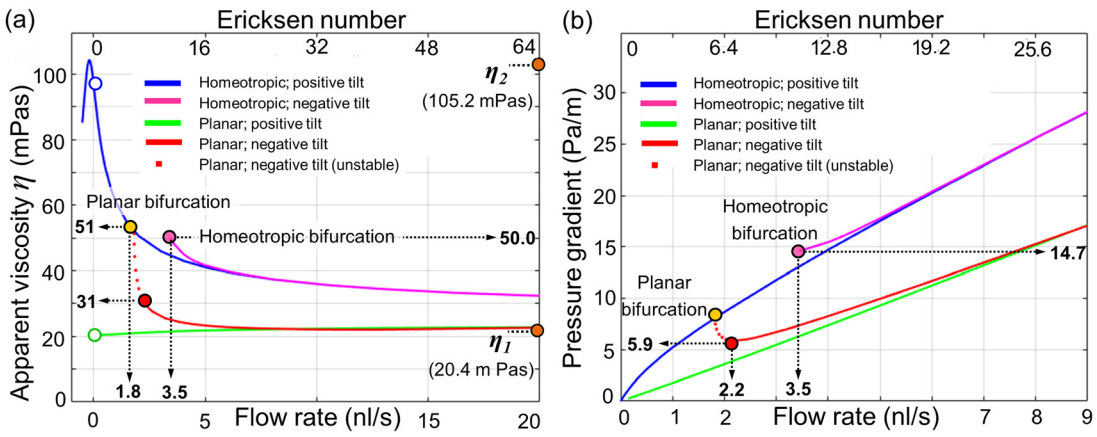

FIG. 10. Nematodynamic bifurcations in capillary flows. Apparent viscosity (a) and pressure gradient (b) plotted as a function of the flow rate for the director configurations plotted in the Figs. 3, 5, and 7 and visualized in Figs. 4, 6, 8, respectively, for homeotropic and uniform planar anchoring conditions. The values of the Miesowicz viscosities are explained in Sec. III. The corresponding Ericksen numbers are shown at the top of the respective plots.

angle can arise when elastic torque plays a comparable role, for instance at moderate or low Ericksen number flow, as well as in the neighborhood of confining boundaries. Such deviations could also arise at transitions between flow states, in non-stationary flows, anchoring-induced symmetry breaking or geometric constraints.[28,35,41,52] These conditions for deviations from the Leslie angle are not fulfilled in the case of the negative tilt angles observed by us at the center of the capillary, in stationary flows with an imposed high symmetry and larger Ericksen numbers. But we do not discard these solutions which are plotted in Figs. 4 and 8 and visualized in Figs. 5 and 9. Instead in Sec. V B, we gather evidence of analogous solutions for experimental micro-flows of NLC-s.

Despite the experimental evidence for the occurrence of the negative tilt angle solutions, it would be desirable to check their stability theoretically. Such investigations have been performed with a linear stability analysis of the Pieranski–Guyon instability in planar Couette flow, Taylor–Couette flow and planar Poiseuille flow,[56–59,66] locating the instability quantitatively. However, the investigated solutions were less complex in nature than what we report here, specifically as the velocity and the director fields remain independent of the *Er*. Furthermore, the director fields in previous stability analyses were spatially independent, with the velocity profiles matching those of the corresponding analytical solutions of the simple isotropic case. For our system, i.e., cylindrical capillaries, Lima and Rey investigated the stability against finite perturbations via time evolution by using the transient equations.[35]

Additionally, we note that our rotationally symmetric solutions exist as coaxial director domains. Therefore, the intersection between such coaxial domains can serve as a new boundary condition. For instance, let us consider the solution corresponding to the flow rate of 19.7 nl/s (Fig. 8). If we now apply the same pressure gradient of 38 Pa/m, across a cylinder of radius 226 μm, i.e., where the tilt angle of the director crosses the zero line, we arrive at an effective solution for flow through a capillary of 226 μm radius possessing uniform planar anchoring. The solution possesses the same *Er* as the solution with 2.6 nl/s, thus from a LEP perspective, these two solutions are mutually equivalent. The possibility to construct such inner solution domains for smaller Ericksen numbers indicates that the elastic interactions can dominate in the inner part of the flow even at higher Ericksen numbers. Therefore, one might find solutions showing negative tilt angles in the inner part at higher Ericksen numbers in experiments with suitably chosen initial conditions. Based on this we hypothesize that the experimental realizations of the alternate flow-induced director orientations (deviated from the Leslie angle) could be enabled or hindered by the lower symmetry of channel flow compared to the cylindrical capillary flows.

The higher persistence of the negative tilt angles near the capillary centerline, depicted in the Figs. 8 and 9 for increasing Ericksen numbers, can be explained as well by analyzing the dependence of the competing forces at a distance r from the capillary center. For given input parameters, the tilt angles are solely determined by Eq. (5) which represents the elastic and the viscous flow effects. The LEP excludes gradients in the director field strength, therefore such gradients, alongside disclinations, do not play a role here. The same holds for twist, because it is excluded in the ansatz of Atkin[51] which we followed with Eqs. (2) and (3). Therefore, only splay and bend terms contribute to the elasticity effects, with material parameters k_{11} (splay) and k_{33} (bend), from which the latter is represented in Eq. (5) indirectly by $f(\theta) = k_{11}\cos^2(\theta) + k_{33}\sin^2(\theta)$ due to Eq. (8). They are either independent of r or scaling with $1/r$ or $1/r^2$. The same holds for dimensionless formulations of Eq. (5).[35] The viscous flow effects are covered by the second line, they scale with r, their denominator $g(\theta)$ is plotted in Fig. 2. Therefore, the relative strength of viscous flow forces compared to elasticity forces is not solely determined by the Ericksen number, but, additionally, by the distance r from the capillary center as well. The ratio between elastic and vicsous terms is more in favor for the former near the center, and vice versa near the boundaries. Because the viscous forces prefer the positive Leslie angle, it seems plausible that for higher Ericksen numbers, as in the dashed graph in Fig. 4 and the red graph in Fig. 9, they are able to overcome the elastic forces near the boundary, and thus Leslie angle is obtained here, while near the center the elasticity forces are still strong enough to influence the director field.

B. Comparison with experimental results

Below we discuss two microfluidic experiments in the context of the negative tilt angles suggested in Secs. IV A and IV B. Figure 11 shows experimental (left column) and simulated (right column) 5CB director profiles that emerge within microfluidic devices possessing homeotropic anchoring.[28] The top left panel shows polarized optical image, while the two bottom images were obtained by confocal

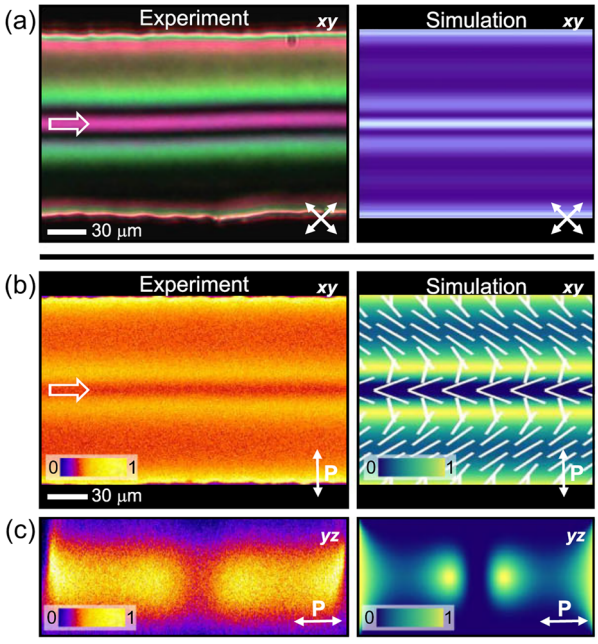

FIG. 11. Tunable nematic director in microfluidic flows. Experimental and simulated microfluidic flow and director profiles for nematic 5CB, adapted with permission from Sengupta *et al.*, Phys. Rev. Lett. **110**, 048303 (2013). Copyright 2013 American Physical Society.[28] The director orientation is indicated by the white lines (right column, middle panel). The left and right columns respectively show the experimental and simulated polarization optical image [panel (a)], confocal polarization fluorescence image [panel (b)], and confocal polarization fluorescence image of the channel cross section [panel (c)]. The flow direction is from left to right, indicated by the arrow heads.

fluorescence polarization microscopy. The director configuration is depicted at the bottom right panel by thin white lines. The director orientation exhibits qualitative similarities to the alternate orientation solution presented in Fig. 4 (for the flow rate of 32 nl/s). Close to the channel walls, the director is oriented close to the Leslie angle, while in the vicinity of the channel center, the director bends against the imposed flow field. However the transition region between the positive and the negative tilt angles reported in their experiment differ from our simulated solution: In our numerical solution the director at this transition region is oriented parallel to the flow direction, while in their experiments, perpendicular.

In Fig. 12, the results of viscosimetric experiments on 5CB in a channel with a large aspect ratio (2 mm × 15 μm) and a length of 4 cm are shown.[45] The viscosity is plotted against the pressure difference between the channel inlet and outlet. The red dots indicate the results for planar anchoring which is relevant in our context. For the smallest pressure difference, a viscosity ∼25 mPa s was observed, which is comparable to the Miesowicz viscosity η_1, as one expects in the limit of zero flow rate. At a pressure difference of 20 mbar, a clear viscosity maximum of 50 mPa s was reported, corresponding to $Er \approx 6$. Upon increasing the pressure difference further, the apparent viscosity falls monotonically, exhibiting expected shear-thinning rheology. While we did not perform corresponding simulations for the channel flow here, we do expect that such simulations would yield similar results, as qualitatively suggested by our simulations for capillary flows [Figs. 10(a) and 13]. Our simulations reproduce the viscosity peak at $Er = 6$ for the negative tilt angle solutions, but not at all for the positive ones. At smaller flow rates, i.e., lower pressure gradients, negative tilt angles are ruled out. Considering the variability in experimental anchoring conditions, we mimicked weak (or variable) anchoring by allowing slightly negative tilt angles at the boundary. This lowered the threshold flow rate for the onset of alternate solution with negative

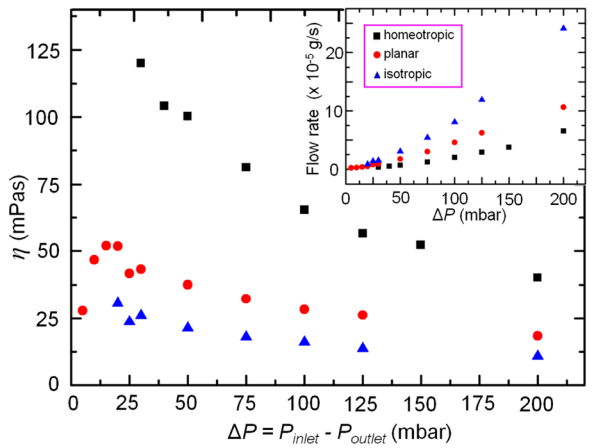

FIG. 12. Dynamic viscosity of flowing nematic 5CB. Adapted from A. Sengupta, Int. J. Mol. Sci. **14**, 22826 (2013). Copyright 2013 Author(s), licensed under a Creative Commons Attribution (CC BY) license,[45] viscosimetric measurements in a high aspect ratio microchannel filled with 5CB for different anchoring and shear rates. The red dots indicate results obtained for the uniform planar anchoring, as investigated in the current work (Figs. 6–9). A close match has been found for the existence of a viscosity maximum around 17 mbar pressure difference (1 mbar = 100 Pa).

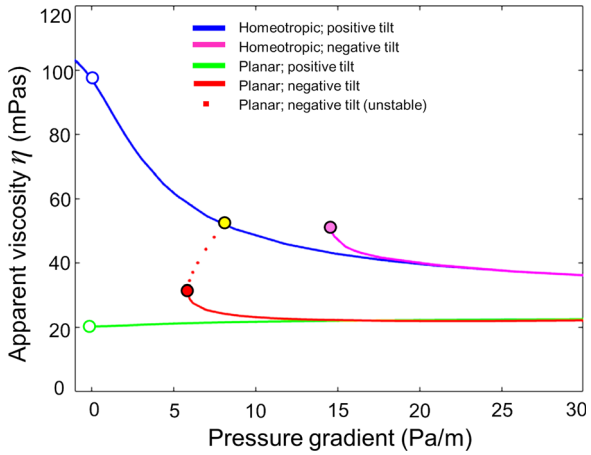

FIG. 13. Harnessing nematodynamic bifurcations in cylindrical capillaries. The nonlinear rheological attributes of NLCs could offer a novel handle to control and manipulate microscale flows. Through a careful choice of material and flow parameters, multi-stable solutions in shear rates and director fields could be obtained at will.

tilt angles. Additionally, we do not exclude that the tilt angles switch sign with changes in the flow rates, underscoring the non-stationarity and perturbations in the flow and director fields. Depending on the manner in which the flow rate is changed, one could induce controlled switching to elicit specific flow-induced solutions. We interpret the close match observed in the viscosity maximum at $Er \approx 6$ as a promising evidence for the occurrence of negative tilt angles in experiments with circular as well as with channel flow geometries, however detailed experimental and theoretical investigations will clearly be needed to uncover the underlying nematodynamic details.

VI. CONCLUSION AND PERSPECTIVES

We presented an overview on the stationary flow of aligning rod-shaped nematic liquid crystal flowing within circular capillaries under strong homeotropic and strong uniform planar anchoring. We spanned the elastic and the viscous dominated regimes, i.e., from small to large Ericksen numbers. Our numerical simulations are based on the Leslie–Ericksen–Parodi theory, with relevant modifications and conditions due to the symmetry of a circular capillary. In contrast to the low complexity of the input, the results show a high complexity including non-monotonic viscosity variation, multiple solutions (having both stable and unstable arms) and nematodynamic bifurcations. Our simulations reveal that the flow field bends the director field toward the Leslie angle for both the anchoring types considered here. The higher the Ericksen number, the closer this convergence is. The employed material parameters possess common properties for rod like nematics, in particular its anisotropic viscosity approaches the minimum for a director field parallel to the flow. Consequently, the viscosities are the lowest for planar anchoring at small flow rates, i.e., when the director field is nearly parallel to the flow direction, increasing monotonically for larger flow rates when the Leslie angle is approached throughout the capillary space. For homeotropic anchoring conditions, the opposite phenomenon is observed, with the exception of flows which are antiparallel to the direction of the static escape configuration. The anisotropic viscosity influences the radial variation

of the nematic flow, i.e., its shear rate profiles, by deviating them from the usual linear profile of the well-known Hagen–Poiseuille flow. At regions with a small angle between flow and director orientation, the shear rates deviate toward larger values, and at angles close to 90° the shear rates approach smaller values.

The highlight of this paper is the discovery of anchoring-dependent nematodynamic bifurcations, which were captured *in silico* within cylindrical capillaries possessing strong homeotropic and uniform planar anchoring conditions. By spanning two orders of flow rates, we identify anchoring-specific threshold flow rates at which alternate flow-director solution emerges (in addition to the expected director field orientation). The bifurcation coordinates on a pressure-viscosity parameter space depend on the nature of surface anchoring on the walls of the cylindrical capillary, and on the driving mechanism of the flow. For strong homeotropic anchoring conditions, the flow bifurcation was found to occur at a pressure gradient of 14.7 Pa/m (for nematic 5CB), with corresponding flow rate 3.5 nl/s and apparent viscosity 50 mPa s. Correspondingly, for Ericksen numbers $Er \geq 11.2$, the second solution emerges. The second solution does not merge with the first solution at the onset threshold, instead its director field and its viscosity are distinct at the onset. A similar observation was found for discotic liquid crystals before.[35] Close to the capillary centerline, the director field orients opposite to the alignment angle. Interestingly, for the planar boundary conditions, the bifurcation coordinates were determined, in addition, by the flow driving mechanism (pressure- vs volume-driven flows). For the pressure-driven flows, the bifurcation occurs at 5.9 Pa/m (corresponding flow rate is 2.2 nl/s) and apparent viscosity 31 mPa s; whereas for volume-driven flows, the bifurcation takes place at a flow rate of 1.8 nl/s (corresponding pressure gradient is 8 Pa/m) and an apparent viscosity of 51 mPa s. In terms of Ericksen numbers, the two additional solutions diverge from each other at $Er = 7$ (flow speed of 2.2 nl/s). The additional solutions do not merge with the standard solution at onset point, with the director fields oriented against the alignment angle. The director field of the additional solutions is bended against the Leslie angle. Overall, the onset of the anchoring-dependent apparent viscosity of nematic 5CB at a given pressure gradient (or flow rate) is coupled to the alternate local director orientations, as summarized in Fig. 13. Our numerical results indicate promising agreement with previously reported experiments on nematic microflows within moderate and high aspect ratio microfluidic devices possessing appropriate surface conditions.[28,45] Cylindrical capillary experiments are under way and the results will be reported elsewhere.

The nonlinear rheology of nematic 5CB is summarized in Fig. 13. The multiplicity, the moderate shear thickening for planar anchoring, the strong shear thinning for both anchoring types, and importantly, the shrinking flow rates with rising pressure gradients under planar anchoring could offer novel handles to control and manipulate microscale flows. Furthermore, by expanding the choice of material parameters, alongside confinement geometry and dimensions, one could tailor multi-stable solutions of shear rates at a given Ericksen number. For sufficiently high shear rates, we expect the experimental viscosities for homeotropic anchoring to be lower than our LEP-based prediction [Figs. 10(a) and 13] for two main reasons: First, at high shear rates the surface extrapolation length even of a strong anchoring will come into play and the molecules close to the surface will get differentially tilted toward the flow direction. Second, the gradients of the tilt angles at the capillary boundary become larger for higher shear rates, which at a certain magnitude (so far unknown) is expected to lower the local order parameter, inducing a local drop in the nematic elasticity. The first case can enable surface anchoring characterizations macroscopically (without the need for polarization microscopy). The second case can reveal the bulk material properties of the nematics, advancing our insights about the limits of the LEP theory. It remains to be explored how the emergence of flow-induced disclination lines—an unavoidable consequence of high Ericksen number flows—impacts the flow fields close to defects in liquid crystals and liquid crystal polymers.[67,68] While this is a challenging step ahead, nematodynamic insights from multiparticle collision approaches, based on tensor order parameters,[69] provide valuable insights (and foresights) toward designing meaningful experimental measurements.

ACKNOWLEDGMENTS

This work was supported by the ATTRACT Investigator Grant (No. A17/MS/11572821/MBRACE) and FNR-CORE Grant (No. C19/MS/13719464/TOPOFLUME/Sengupta) to A.S. from the Luxembourg National Research Fund. The authors thank J. Dhar for lively discussions during different phases of this work.

DATA AVAILABILITY

The data that support the findings of this study are available from the corresponding author upon reasonable request.

REFERENCES

[1]B. Fonseca-Santos, M. Palmira Daflon Gremião, and M. Chorilli, "Nanotechnology-based drug delivery systems for the treatment of Alzheimer's disease," Int. J. Nanomed. **10**, 4981 (2015).
[2]M. Schwartz, G. Lenzini, Y. Geng, P. B. Rønne, P. Y. A. Ryan, and J. P. F. Lagerwall, "Cholesteric liquid crystal shells as enabling material for information-rich design and architecture," Adv. Mater. **30**, 1707382 (2018).
[3]K. Nayani, Y. Yang, H. Yu, P. Jani, M. Mavrikakis, and N. Abbott, "Areas of opportunity related to design of chemical and biological sensors based on liquid crystals," Liq. Cryst. Today **29**, 24–35 (2020).
[4]R. Zhang, A. Mozaffari, and J. J. de Pablo, "Autonomous materials systems from active liquid crystals," Nat. Rev. Mater. **6**, 437 (2021).
[5]J. G. Cuennet, A. E. Vasekis, L. De Sio, and D. Psaltis, "Optofluidic modulator based on peristaltic nematogen microflows," Nat. Photonics **5**, 234 (2011).
[6]M. Nikkhou, M. Škarabot, S. Čopar *et al.*, "Light-controlled topological charge in a nematic liquid crystal," Nat. Phys. **11**, 183 (2015).
[7]Y. Luo, F. Serra, and K. J. Stebe, "Experimental realization of the "lock-and-key" mechanism in liquid crystals," Soft Matter **12**, 6027 (2016).
[8]I. I. Smalyukh, "Knots and other new topological effects in liquid crystals and colloids," Rep. Prog. Phys. **83**, 106601 (2020).
[9]C. Peng, T. Turiv, Y. Guo, Q. H. Wei, and O. D. Lavrentovich, "Command of active matter by topological defects and patterns," Science **354**, 882 (2016).
[10]C. Guo, J. Wang, F. Cao, R. J. Lee, and G. Zhai, "Lyotropic liquid crystal systems in drug delivery," Drug Discovery Today **15**, 1032 (2010).
[11]I. H. Lin, D. S. Miller, P. J. Bertics *et al.*, "Endotoxin-induced structural transformations in liquid crystalline droplets," Science **332**, 1297 (2011).
[12]J. Fishers and A. G. Fredrickson, "Interfacial effects on the viscosity of a nematic mesophase," Mol. Cryst. **8**, 267 (1969).
[13]A. Sengupta, S. Herminghaus, and C. Bahr, "Liquid crystal microfluidics: Surface, elastic and viscous interactions at micro-scales," Liq. Cryst. Rev. **2**, 73 (2014).
[14]O. D. Lavrentoich, "Transport of particles in liquid crystals," Soft Matter **10**, 1264 (2014).

[15]M. Miesowicz, "The three coefficients of viscosity of anisotropic liquids," Nature **158**, 27 (1946).
[16]P. Pieranski and E. Guyon, "Transverse effects in nematic flows," Phys. Lett. A **49**, 237 (1974).
[17]J. Dhar and S. Chakraborty, "Spontaneous electrorheological effect in nematic liquid crystals under Taylor–Couette flow configuration," Phys. Fluids **29**, 092008 (2017).
[18]A. Poddar, J. Dhar, and S. Chakraborty, "Electro-osmosis of nematic liquid crystals under weak anchoring and second-order surface effects," Phys. Rev. E **96**, 013114 (2017).
[19]1J. Quintans Carou, B. R. Duffy, N. J. Mottram, and S. K. Wilson, "Shear-driven and pressure-driven flow of a nematic liquid crystal in a slowly varying channel," Phys. Fluids **18**, 027105 (2006).
[20]O. Wiese, D. Marenduzzo, and O. Henrich, "Microfluidic flow of cholesteric liquid crystals," Soft Matter **12**, 9223 (2016).
[21]S. A. Jewell, S. L. Cornford, F. Yang, P. S. Cann, and J. Sambles, "Flow-driven transition and associated velocity profiles in a nematic liquid-crystal cell," Phys. Rev. E **80**, 04106 (2009).
[22]A. Sengupta, C. Bahr, and S. Herminghaus, "Topological microfluidics for flexible micro-cargo concepts," Soft Matter **9**, 7251 (2013).
[23]T. Stieger, H. Agha, M. Schoen, M. G. Mazza, and A. Sengupta, "Hydrodynamic cavitation in Stokes flow of anisotropic fluids," Nat. Commun. **8**, 15550 (2017).
[24]A. Sengupta, *Topological Microfluidics* (Springer International Publishing, Switzerland, 2013), ISBN: 978-3-319–00857-8.
[25]D. Banerjee, A. Souslov, A. G. Abanov, and V. Vitelli, "Odd viscosity in chiral active fluids," Nat. Commun. **8**, 1573 (2017).
[26]R. Zhang *et al.*, "Spatiotemporal control of liquid crystal structure and dynamics through activity patterning," Nat. Mater. **20**, 875 (2021).
[27]J.-C. Eichler, R. A. Skutnik, A. Sengupta, M. G. Mazza, and M. Schoen, "Emergent biaxiality in nematic microflows illuminated by a laser beam," Mol. Phys. **117**, 3715 (2019).
[28]A. Sengupta, U. Tkalec, M. Ravnik, J. Yeomans, C. Bahr, and S. Herminghaus, "Liquid crystal microfluidics for tunable flow shaping," Phys. Rev. Lett. **110**, 048303 (2013).
[29]L. Giomi, Ž. Kos, M. Ravnik, and A. Sengupta, "Cross-talk between topological defects in different fields revealed by nematic microfluidics," Proc. Natl. Acad. Sci. U. S. A. **114**, E5771 (2017).
[30]W. Pomp *et al.*, "Cytoskeletal anisotropy controls geometry and forces of adherent cells," Phys. Rev. Lett. **12**, 178101 (2018).
[31]Ž. Kos and M. Ravnik, "Elementary flow field profiles of micro-swimmers in weakly anisotropic nematic fluids: Stokeslet, stresslet, rotlet and source flows," Fluids **3**, 15 (2018).
[32]S. Liu, S. Shankar, M. C. Marchetti, and Y. Wu, "Viscoelastic control of spatiotemporal order in bacterial active matter," Nature **590**, 80–84 (2021).
[33]T. Tsuji and A. D. Rey, "Effect of long range order on sheared liquid crystalline materials: Flow regimes, transitions, and rheological phase diagrams," Phys. Rev. E **62**, 8141 (2000).
[34]A. D. Rey and M. M. Denn, "Dynamical phenomena in liquid-crystalline materials," Annu. Rev. Fluid Mech. **34**, 233 (2002).
[35]L. R. P. de Andrade Lima and A. D. Rey, "Poiseuille flow of Leslie–Ericksen discotic liquid crystals: Solution multiplicity, multistability, and non-Newtonian rheology," J. Non-Newtonian Fluid Mech. **110**, 103 (2003).
[36]A. D. Rey, "Liquid crystal models of biological materials and processes," Soft Matter **6**, 3402 (2010).
[37]E. V. Alonso, A. A. Wheeler, and T. J. Sluckin, "Nonlinear dynamics of a nematic liquid crystal in the presence of a shear flow," Proc. R. Soc. London, Ser. A **459**, 195 (2003).
[38]C. Denniston, E. Orlandini, and J. M. Yeomans, "Simulations of liquid crystals in Poiseuille flow," Comput. Theor. Polym. Sci. **11**, 389 (2001).
[39]M. Ravnik and J. M. Yeomans, "Confined active nematic flow in cylindrical capillaries," Phys. Rev. Lett. **110**, 026001 (2013).
[40]V. M. O. Battista, M. L. Blow, and M. M. Telo da Gama, "The effect of anchoring on the nematic flow in channels," Soft Matter **11**, 4674 (2015).
[41]T. G. Anderson, E. Mema, L. Kondic, and I. J. Cummings, "Transitions in Poiseuille flow of nematic liquid crystal," Int. J. Nonlinear Mech. **75**, 15 (2015).
[42]S. Mondal, S. I. M. Griffiths, F. Charlet, and A. Majumdar, "Flow and nematic director profiles in a microfluidic channel: The interplay of nematic material constants and backflow," Fluids **3**, 39 (2018).
[43]J. Walton, G. McKay, M. Grinfeld, and N. J. Mottram, "Pressure-driven changes to spontaneous flow in active nematic liquid crystals," Eur. Phys. J. E **43**, 1 (2020).
[44]H. Zhou and G. Forest, "Nematic liquids in weak capillary Poiseuille flow: Structure scaling laws and effective conductivity implications," Int. J. Numer. Anal. Model. **4**, 460 (2007).
[45]A. Sengupta, "Tuning fluidic resistance via liquid crystal microfluidics," Int. J. Mol. Sci. **14**, 22826 (2013).
[46]F. C. Frank, "Liquid crystals. On the theory of liquid crystals," Discuss. Faraday Soc. **25**, 19 (1958).
[47]P. G. DeGennes and J. Prost, *The Physics of Liquid Crystals*, 2nd ed. (Oxford University Press, Inc., New York, 1993).
[48]I. W. Stewart, *The Static and Dynamic Continuum Theory of Liquid Crystals: A Mathematical Introduction*, 1st ed. (CRC Press, Boca Raton, 2004).
[49]P. Oswald and P. Pieranski, *Nematic and Cholesteric Liquid Crystals* (CRC Press, 2005), ISBN: 9780429215742.
[50]C. Gähwiller, "Temperature dependence of flow alignment in nematic liquid crystals," Phys. Rev. Lett. **28**, 1554 (1972).
[51]R. J. Atkin, "Poiseuille flow of liquid crystals of the nematic type," Arch. Ration. Mech. Anal. **38**, 224 (1970).
[52]H. C. Tseng, D. L. Silver, and B. A. Finnlayson, "Application of the continuum theory to nematic liquid crystals," Phys. Fluids **15**, 1213 (1972).
[53]P. Pieranski and E. Guyon, "Instability of certain shear flows in nematic liquids," Phys. Rev. A **9**, 404 (1974).
[54]E. Guyon and P. Pieranski, "Poiseuille flow instabilities in nematics," J. Phys., Colloq. **36**, 203 (1975).
[55]I. Janossy, P. Pieanski, and E. Guyon, "Poiseuille flow in nematics: Experimental study of the instabilities," J. Phys. **37**, 1105 (1976).
[56]E. Dubois-Violette, E. Guyon, I. Janossy, P. Pieranski, and P. Manneville, "Theory and experiments on plane shear flow instabilities in nematics," J. Mec. **16**, 733 (1977).
[57]P. Manneville, "Non-linearities and fluctuations at the threshold of a hydrodynamic instability in nematic liquid crystals," J. Phys. France **39**, 911 (1978).
[58]P. Manneville, "Theoretical analysis of Poiseuille flow instabilities in nematics," J. Phys. **40**, 713 (1979).
[59]P. E. Cladis and M. Kléman, "Non-singular disclination of strength S = +1 in nematics," J. Phys. **33**, 591 (1972).
[60]R. B. Meyer, "On the existence of even indexed disclinations in nematic liquid crystals," Philos. Mag. **27**, 405 (1973).
[61]J. Dhar and S. Chakraborty, "Electrically modulated capillary filling imbibition of nematic liquid crystals," Phys. Rev. E **97**, 043107 (2018).
[62]P. Steffen, E. Stellamanns, M. Sprung, F. Westermeier, and A. Sengupta, "SAXS study on nematic microflows in cylindrical micro-capillaries" (unpublished).
[63]A. Sengupta, U. Tkalec, and C. Bahr, "Nematic textures in microfluidic environment," Soft Matter **7**, 6542 (2011).
[64]A. Sengupta, B. Schulz, E. Ouskova, and C. Bahr, "Functionalization of microfluidic devices for investigation of liquid crystal flows," Microfluid. Nanofluid. **13**, 941 (2012).
[65]J. Stoer and R. Bulirsch, *Introduction to Numerical Analysis* (Springer-Verlag, New York, 1980).
[66]P. J. Barratt, J. M. Manley, and V. A. Nye, "A linear analysis of instabilities in Couette flow of nematic liquid crystals," Rheol. Acta **26**, 343 (1987).
[67]G. Sgalari and L. G. Leal, "Texture evolution of sheared liquid crystalline polymers: Numerical predictions of roll-cells instability, director turbulence, and striped texture with a molecular mode," J. Rheol. **47**, 1417 (2003).
[68]D. H. Klein and L. G. Leal, "Three-dimensional shear-driven dynamics of polydomain textures and disclination loops in liquid crystalline polymers," J. Rheol. **52**, 837 (2008).
[69]S. Mandal and M. G. Mazza, "Multiparticle collision dynamics for tensorial nematodynamics," Phys. Rev. E **99**, 063319 (2019).